

PULSAR OBSERVATIONS AT LOW LATITUDES AND LOW FREQUENCIESCarlos O. Lousto,¹R.Missel,² E.Zubieta,^{3,4} S.del Palacio,^{4,5} F.Garcia,⁴ G.Gancio,⁴ L.Wang,² S.B.Araujo Furlan,^{6,7} J.A.Combi⁸

RESUMEN

La colaboración PuMA (Pulsar monitoring in Argentina) entre el Instituto Argentino de Radioastronomía (IAR) y el Rochester Institute of Technology (RIT) ha estado observando púlsares en el hemisferio sur desde el año 2017 con una cadencia aproximadamente diaria utilizando las dos antenas recientemente restauradas del IAR en la banda-L (1400MHz). Aquí presentamos una breve reseña de los primeros resultados del programa PuMA para observar fenómenos transitorios, como los magnetares y los púlsares con anomalías en sus períodos, así como medidas muy precisas del tiempo de llegada de los pulsos provenientes de púlsares con períodos de milisegundos. El acceso a observaciones en más baja radiofrecuencias, donde la mayoría de los púlsares tienen un espectro de radiación más brillante, nos permitiría observar con suficiente precisión nuevos púlsares, que actualmente presentan demasiado ruido de fondo en la banda-L. Así, identificamos una docena de púlsares de interés, que presentan anomalías en sus períodos, y que podrían ser observado por el nuevo instrumento proyectado por el IAR, el Multipurpose Interferometer Array (MIA), en la banda de los 400MHz. También discutimos aquí la importancia de las observaciones y el estudio de pulsos individuales (y sus dificultades) para mejorar la precisión de la medida de los tiempos de arribo de los pulsos de púlsares de milisegundos y la aplicación de técnicas de aprendizaje automático de inteligencia artificial para la búsqueda de FRBs (Fast Radio Burst – ráfagas rápidas de radio) en la gran cantidad de datos colectados por el IAR desde el año 2017.

ABSTRACT

The Pulsar Monitoring in Argentina (PuMA) is a collaboration between the Argentine Institute for Radioastronomy (IAR) and the Rochester Institute of Technology (RIT) that since 2017 has been observing southern sky pulsars with high cadence using the two restored IAR antennas in the L-Band (1400MHz). We briefly review the first set of results of this program to study transient phenomena, such as magnetars and glitching pulsars, as well as to perform precise timing of millisecond pulsars. Access to lower frequency bands, where most of the pulsars are brighter, would allow us to reach additional pulsars, currently buried into the background noise. We identify two dozen additional glitching pulsars that could be observable in the 400MHz band by the IAR’s projected Multipurpose Interferometer Array (MIA). We also discuss the relevance and challenges of single-pulse pulsar timing at low frequencies and the search for Fast Radio Burst (FRB) in the collected data since 2017 using machine learning techniques.

Key Words: Instrumentation: detectors — methods: observational — methods: statistical — pulsars: Vela — pulsars: PSR J0437–4715

¹Center for Computational Relativity and Gravitation (CCRG), School of Mathematical Sciences, Rochester Institute of Technology, 85 Lomb Memorial Drive, Rochester, New York 14623, USA.

²Golisano College of Computing and Information Sciences, Rochester Institute of Technology Rochester, NY 14623, USA.

³Facultad de Ciencias Astronómicas y Geofísicas, Universidad Nacional de La Plata, Paseo del Bosque, B1900FWA La Plata, Argentina.

⁴Instituto Argentino de Radioastronomía (CCT La Plata, CONICET; CICIPBA; UNLP), C.C.5, (1894) Villa Elisa, Buenos Aires, Argentina.

⁵Department of Space, Earth and Environment, Chalmers University of Technology, Sweden. SE-412 96 Gothenburg.

⁶Instituto de Astronomía Teórica y Experimental, CONICET-UNC, Laprida 854, X5000BGR – Córdoba, Argentina.

⁷Facultad de Matemática, Astronomía, Física y Com-

1. INTRODUCTION

The Argentine Institute of Radio astronomy (IAR) was founded in 1962 as a pioneer radio observatory in South America with two 30-meter parabolic single-dish radio antennas (Fig. 1). Antenna 1 (A1) saw its first light in 1966 whereas Antenna 2 (A2) was built later in 1977. The IAR’s initial purpose was to perform a high sensitivity survey of neutral hydrogen ($\lambda = 21$ cm) in the southern hemisphere; this survey ended satisfactorily in the year 2000 with high-impact publications in collaboration, UNC. Av. Medina Allende s/n, Ciudad Universitaria, CP:X5000HUA - Córdoba, Argentina.

⁸Departamento de Física (EPS), Universidad de Jaén, Campus Las Lagunillas s/n, A3, 23071 Jaén, Spain.

ration with German and Dutch institutions (Testori et al. 2001; Bajaja et al. 2005; Kalberla et al. 2005). (See G. Romero’s contribution to this volume for more historical details).

Although the IAR has been a center of intense scientific and technological activity since its foundation, the radio antennas had not been employed in any scientific project since 2001. The PuMA⁹ (Pulsar Monitoring in Argentina) is a new collaboration of scientists and technicians from the IAR and the Rochester Institute of Technology (RIT) dedicated to the formation of human resources for observations, data analysis, and pulsar astrophysics studies. This project represents the first systematic pulsar timing observations in South America and the beginning of pulsar science in Argentina. (See P. Benaglia’s contribution to this volume for other independent research projects being carried out at IAR).

Since 2017 the IAR antennas have been upgraded to conduct high-quality radio astronomy (Gancio et al. 2020) to enable science projects for the first time in over fifteen years. These projects include: i) Pulsar timing and gravitational waves, ii) Targeted pulsar studies for continuous gravitational waves detection from laser interferometry, iii) Magnetars, iv) Glitches and young pulsars, v) Fast-radio-burst observations, vi) Interstellar medium scintillation, vii) Tests of gravity with pulsar timing.



Fig. 1. View of IAR antennas, A2 (left) and A1 (right).

2. MAIN RESULTS

2.1. J0437–4715 first timing campaign

We presented the first-year of high-cadence, long-duration observations of the bright millisecond pulsar J0437–4715 obtained in the IAR in (Sosa Fiscella et al. 2021). Using the two single-dish 30 m radio antennas, we gathered more than 700 hr of good-quality data with timing precision better than 1 μ s.

⁹<http://puma.iar.unlp.edu.ar>

We characterized the white and red timing noise in IAR’s observations, we quantified the effects of scintillation, and we performed single-pulsar searches of continuous gravitational waves, setting constraints in the nHz– μ Hz frequency range. We thus demonstrated IAR’s potential for performing pulsar monitoring in the 1.4 GHz radio band for long periods of time with a nearly daily cadence. In particular, we concluded that the ongoing observational campaign of J0437–4715 can contribute to increase the sensitivity of the existing pulsar-timing arrays.

The characterization of the observations used in this work are summarized in Table 1.

TABLE 1

J0437–4715 OBSERVATIONS

	A1	A2
Number of observations	170	197
MJD start–MJD finish	58596.7 – 58999.6	
Total observation time [h]	391	393
Central frequency [MHz]	1400-1428	1428
Bandwidth (BW) [MHz]	112	56
Polarization modes	1	2
Frequency channels (n_{chan})	64/128	64
Time resolution [μ s]	73.14	73.14
Phase bins (n_{bin})	512/1024	512/1024

Fig. 2 shows the timing residuals of the observations taken with each antenna.

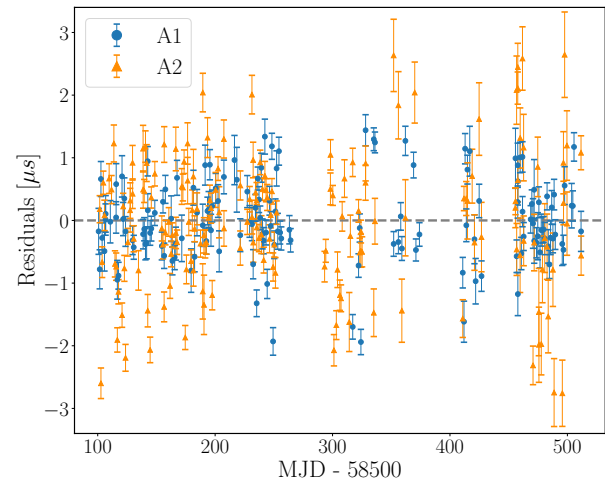


Fig. 2. Timing residuals for the complete data set for A1 and A2.

A single supermassive binary black-hole system produces “continuous” gravitational waves because the system does not evolve notably over the few years of a pulsar-timing data set. We used the Python

package `Hasasia` (Hazboun et al. 2019) to calculate the single-pulsar sensitivity curve of our data set of J0437–4715 for detecting a deterministic gravitational waves source averaged over its initial phase, inclination, and sky location. The resulting sensitivity curve is shown in Fig. 3. It is readily seen that there is a loss of sensitivity at a frequency of $(1 \text{ yr})^{-1}$, caused by fitting the pulsar’s position, and at a frequency of $(\text{PB})^{-1} \sim 2 \mu\text{Hz}$ (with PB the orbital period), caused by fitting the orbital parameters of the binary system. The additional spikes seen at frequencies higher than $(\text{PB})^{-1}$ correspond to harmonics of the binary orbital frequency.

For comparison, we used the code `ENTERPRISE` (Ellis et al. 2019) to perform a fixed-frequency Markov chain Monte Carlo procedure at four different frequencies. We obtained a posterior distribution for $\log_{10} h_{\text{gw}}$ at each of these frequencies with a mean value in great agreement with the curve obtained with `Hasasia`, as shown in Fig. 3.

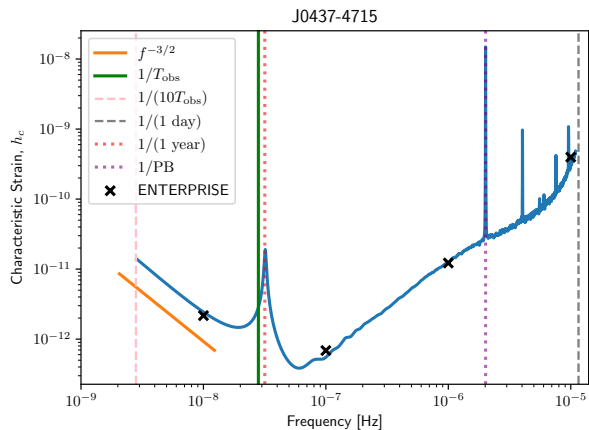


Fig. 3. Sensitivity curve for J0437–4715 using 1.1 yr observations at IAR, including pulsar noise characteristics, for a single deterministic gravitational wave source averaged over its initial phase, inclination, and sky location (A1+A2; blue curve). The vertical green line corresponds to a frequency of $1/T_{\text{obs}}$, the dotted red line to $1/T_{\text{yr}}$ and the dotted purple line to $1/\text{PB}$ (orbital period). The black crosses correspond to the mean values of the $\log_{10} h_{\text{gw}}$ distributions obtained using `ENTERPRISE`.

These first results on gravitational waves sensitivity are encouraging, though we still need to achieve a sensitivity of at least a factor 10 higher in order to observe even the most favourable supermassive black hole binary merger events. For instance, the six billion solar mass source of 3C 186 at $z \approx 1$ produced a gravitational wave amplitude of $h \sim 10^{-14}$ at the time of arrival to our Galaxy, roughly a million years ago (Lousto et al. 2017). The goal of the PuMA

collaboration is to continue analyzing the additional years since 2020 of J0437–4715 observations using the traditional timing techniques as well as the single pulse studies, as performed for Vela pulsar (Lousto et al. 2022).

2.2. Single pulses analysis with machine learning techniques: Vela pulsar

In (Lousto et al. 2022) we studied individual pulses of Vela (PSR B0833-45 / J0835-4510) from daily observations of over three hours (around 120,000 pulses per observation), performed simultaneously with the two radio telescopes at the IAR. We selected 4 days of observations in January–March 2021 and study their statistical properties with machine learning techniques. We first used density based DBSCAN clustering techniques, associating pulses mainly by amplitudes, and find a correlation between higher amplitudes and earlier arrival times. We also found a weaker correlation with the mean width of the pulses. We identified clusters of the so-called mini-giant pulses, with ~ 10 times the average pulse amplitude. We then performed an independent study, with Self-Organizing Maps (SOM) clustering techniques. We use Variational AutoEncoder (VAE) reconstruction of the pulses to separate them clearly from the noise and select one of the days of observation to train VAE and applied it to the rest of the observations. We used SOM to determine 4 clusters of pulses per day per radio telescope and concluded that our main results are robust and self-consistent. These results support models for emitting regions at different heights (separated each by roughly a hundred km each) in the pulsar magnetosphere. We also modeled the pulses amplitude distribution with interstellar scintillation patterns at the inter-pulses time-scale finding a characterizing exponent $n_{\text{ISS}} \sim 7 - 10$.

We analyzed observations on January, 21th, 24th and 28th, and on March 29th, 2021, performed concurrently with both radio telescopes for over three hours. The number of single-pulses in each observation is given in Table 2.

2.2.1. Scintillation

Scintillation due to the interstellar media can change the intensity of the pulses. Fig. 4 shows a histogram of the projected pulse S/N for A1 and A2. The line shows the estimated probability density function (PDF) from scintillation (Cordes & Chernoff 1997),

$$f_S(S|n_{\text{ISS}}) = \frac{(S n_{\text{ISS}}/S_0)^{n_{\text{ISS}}}}{S \Gamma(n_{\text{ISS}})} \exp\left(\frac{-S n_{\text{ISS}}}{S_0}\right) \Theta(S), \quad (1)$$

TABLE 2

DATE, NUMBER OF SINGLE PULSES, MJD
AND INSTANTANEOUS PERIOD AT THE
BEGINNING OF EACH OBSERVATION

Day 2021	initial MJD	#pulses	P_{inst} [ms]
Jan. 21	59235.128553	121495	89.407366
Jan. 24	59239.117013	119448	89.407676
Jan. 28	59242.088680	128999	89.407915
Mar. 29	59302.943356	128999	89.413017

where n_{ISS} is the number of scintles, S_0 is the mean value of the signal S (i.e., $S_0 = \langle S/N \rangle$), and Θ is the Heaviside step function. Since $S \propto T_{\text{peak}}$ (Lorimer & Kramer 2012), it follows that T_{peak} also obeys the PDF in Eq. (1). Here we will explore the possibility of modeling the individual pulses amplitude distribution entirely in terms of a pure interstellar scintillation effect. We therefore calculate n_{ISS} by fitting the observed single pulse peak amplitudes for each Radio telescope. We also normalize the number of observations in each bin by the total number of single pulses in each observation.

As a result, for Vela, we find $n_{\text{ISS}} \sim 6.6 - 7.4$ with A1 and $n_{\text{ISS}} \sim 9 - 10$ for A2. We also note the large value of the n_{ISS} found in comparison to the typical $n_{\text{ISS}} < 2$ found for longer time scales and different radio-frequencies. (Cordes 2000) found two scintillation scales observing Vela at 2.5 GHz of 15s and 26s. Rescaling those scales to our observing frequency, 1400 MHz, we find time scales of $\Delta t_{d,1} = 7.48$ s and $\Delta t_{d,2} = 12.97$ s. Likewise we rescale the scintillation bandwidths to 1400 MHz, and find $\Delta \nu_{d,1} = 3.84$ MHz and $\Delta \nu_{d,2} = 6.49$ MHz, respectively. We can now compare our values of n_{ISS} with theoretical estimations via the formula (Cordes & Chernoff 1997)

$$n_{\text{ISS}} \approx \left(1 + \eta_t \frac{T}{\Delta t_d}\right) \left(1 + \eta_\nu \frac{BW}{\Delta \nu_d}\right) \quad (2)$$

where η_t and η_ν are filling factors ~ 0.25 . The estimated n_{ISS} for $T = 0.089$ s A1 ($BW = 112$ MHz) and for A2 ($BW = 56$ MHz) are $n_{\text{ISS},1} = 8.3$ and $n_{\text{ISS},1} = 4.7$ for A1 and A2 respectively, and $n_{\text{ISS},2} = 5.3$ for A1 and $n_{\text{ISS},2} = 3.2$ for A2.

We then conclude that n_{ISS} over a shorter (0.089 seconds) timescale is expected to be smaller than measured for A2 and polarization dependent (values roughly match the one-polarization measures of A1). We also find a relatively good agreement between the observational data and the theoretical PDF, showing that Eq. (1) holds valid even at such short timescales. Nonetheless, we also note an excess in the number

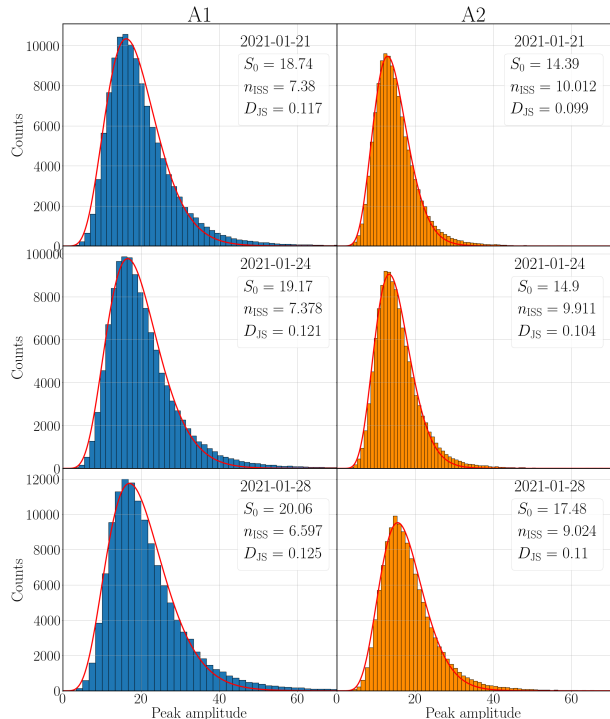


Fig. 4. Histograms of projected pulse amplitude for J0835–4510 for A1 (left column) and A2 (right column) for the January 2021 observations. The curve shows the estimated scintillation distribution from fitting n_{ISS} in Eq. (1).

of high-amplitude single pulses that cannot be explained solely on the basis of scintillation. Those represent several thousands of pulses, and leave room for its interpretation in terms of pulsar intrinsic mini-giant pulses.

2.2.2. Self-Organizing Map (SOM) techniques and results

In deep learning literature, there are various unsupervised approaches to learn or capture the representations of the data. The most common ones include the autoencoder and its variants, a class of deep learning algorithms that take in the input and try to reconstruct the same input by passing it through the low-dimensional bottleneck subjected to different regularizations (e.g., sparsity). In our case, we consider a variational autoencoder (VAE) which is a probabilistic model with stochastic latent space (Kingma & Welling 2014).

After training the VAE, we consider the Self-Organizing Map (SOM) for unsupervised clustering. SOM is a type of neural network that produces a low-dimensional map (2D), a discretized representation of the input samples. We present the schematic

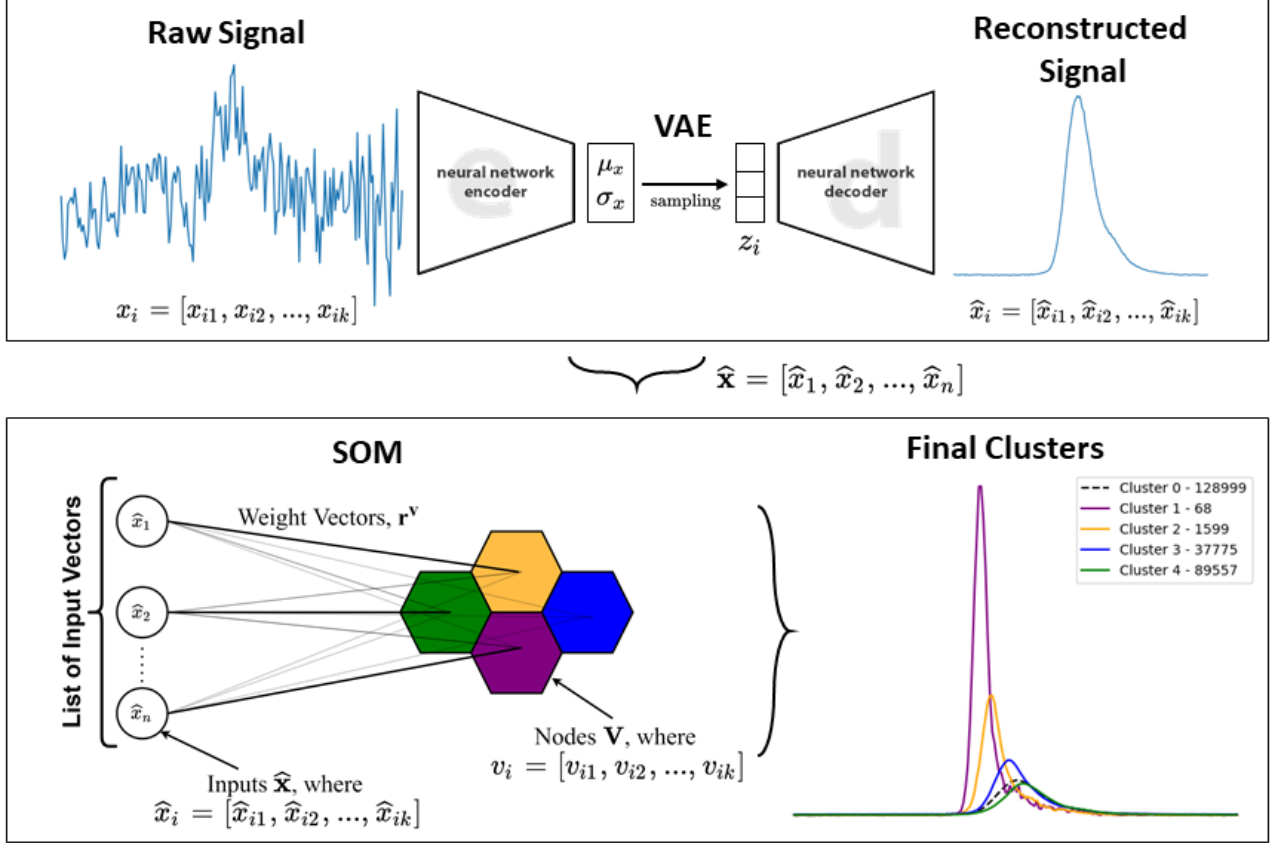


Fig. 5. Schematics of the VAE reconstruction of all N individual pulses signals and of SOM clustering.

diagram of VAE and usage of SOM for clustering in Fig. 5.

In Fig. 6 we display, as a sample, the average value of the pulses in each SOM cluster for each Radio telescope observation on 2021-01-21. Those have been obtained by first applying a reconstruction of the raw pulses with the VAE technique, for which we have used the reconstruction of our best day of observation (2021-01-28) as a training case to apply to the rest of the days of observation. This training has been applied for each antenna individually. SOM allows us to specify then the number of clusters we seek to subdivide the whole set. We have studied several possible cases, 4, 6, 10, 25, 100 clusters, finding that the simplest four cluster analysis presents the most robust results.

We use the SOM clustering to determine four relevant sets of pulses characteristics that seem to linearly array along the emission regions of the magnetosphere (See Fig. 7) separated by roughly 100km each.

2.2.3. Geometrical modeling of the cluster components

As presented Sec. 2.2.1, the excess of high amplitude pulses cannot be explained solely due to effects of scintillation. In Sec. 2.2.2 we also find that each cluster has a different average peak location, with brighter pulses arriving earlier. Therefore, following the classic work of (Krishnamohan & Downs 1983), we may attribute these variations in pulse amplitude and location to different altitudes in the neutron star magnetosphere where the pulses of each cluster are emitted. To this end, we measure the displacement of each cluster peak location relative to the average pulse location, and then relate those pulse displacements to differences in the emission altitude by

$$h - \bar{h} = \frac{x - \bar{x}}{n_{\text{bins}}} cP, \quad (3)$$

where x and h are the cluster peak location and altitude in the magnetosphere, \bar{x} and \bar{h} are the average peak location and the average altitude (corresponding to cluster 0), n_{bins} is the number of time bins in each pulse (in our case, 1220), and P is the pulsar rotational period. Fig.7 displays the results of applying

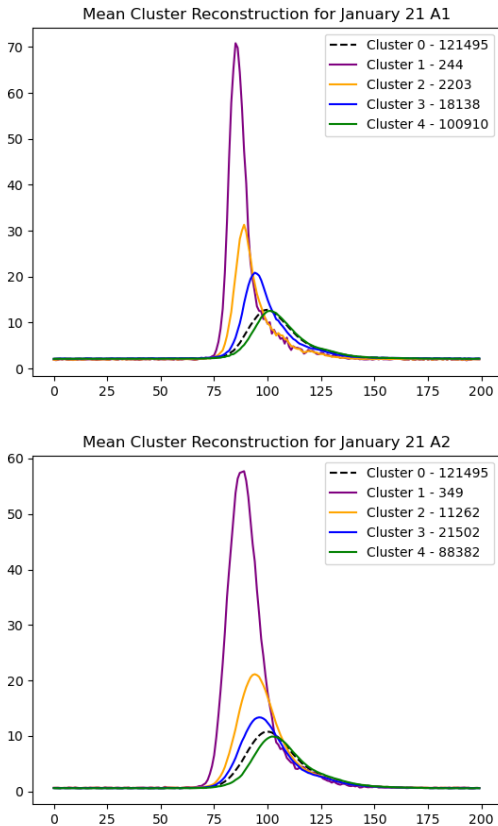


Fig. 6. Distribution of the SOM clustering average signals for the observations 2021-01-21. Radio telescope A1 on top and Radio telescope A2 on bottom with respective VAE training performed on the January 28 observation.

this model to each of the four days of observation for each antenna. The right hand side ordinate gives the components distances to the average pulse reference height in the pulsar magnetosphere. We note the consistency between the components for each of the four days and for each individual antenna’s observations. The four components appear to be almost equidistant (this maybe an effect of the SOM clustering method) and roughly of the order of ~ 100 kilometers.

2.3. Glitching pulsars monitoring program

The PuMA collaboration has been monitoring with high cadence a set of pulsars from the southern hemisphere that had shown glitches before (Gancio et al. 2020). The Vela Pulsar (PSR B0833–45 / PSR J0835–4510) is one of the most active pulsars in terms of glitching, counting 21 in the last 50+ years. Our early monitoring allowed us to detect a large glitch on 2019 February 1st (Lopez

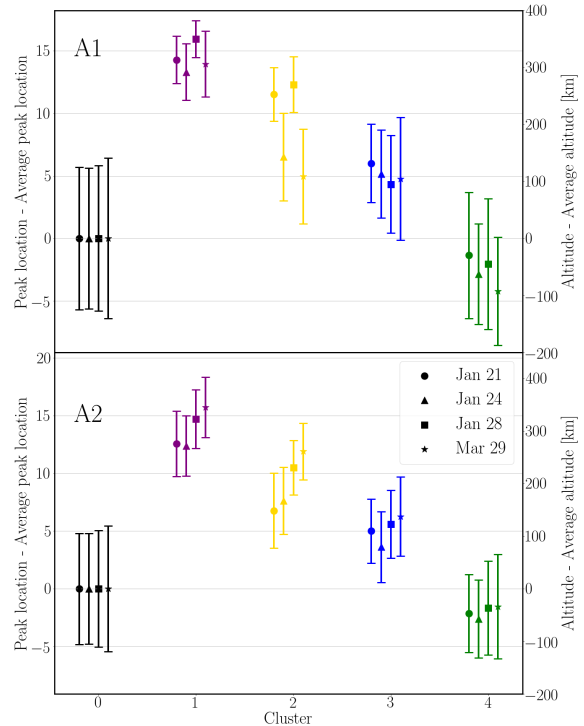


Fig. 7. Peak location and magnetosphere altitude, with the corresponding error bars, for each of the pulse clusters presented in Sec. 2.2.2.

Armengol et al. 2019), measured with observations three days before and three days after the event. In addition to Vela, we are currently systematically monitoring the pulsars mentioned in (Gancio et al. 2020), J0742–2822, J1048–5832, J1644–4559, J1721–3532, J1731–4744, J1740–3015, and plan to extend this list to other accessible (bright) glitching pulsars.

In (Zubieta et al. 2023) we reported on the new results of a systematic monitoring of southern glitching pulsars at the Argentine Institute of Radioastronomy that started in the year 2019. We detected a major glitch in the Vela pulsar (PSR J0835–4510) and two small-glitches in PSR J1048–5832. For each glitch, we presented the measurement of glitch parameters by fitting timing residuals. We then made an individual pulses study of Vela in observations before and after the glitch. We selected 6 days of observations around the major glitch on 2021 July 22 and study their statistical properties with machine

learning techniques. We used Variational AutoEncoder (VAE) reconstruction of the pulses to separate them clearly from the noise. We performed a study with Self-Organizing Maps (SOM) clustering techniques to search for unusual behavior of the clusters during the days around the glitch not finding notable qualitative changes. We have also detected and confirmed recent glitches in PSR J0742–2822 and PSR J1740–3015.

When a glitch occurs, the pulsar suffers a sudden jump in its rotation frequency. This spin up can be introduced in the timing model as a change in the phase of the pulsar modeled as (Mcculloch et al. 1987)

$$\phi_g(t) = \Delta\phi + \Delta\nu_p(t - t_g) + \frac{1}{2}\Delta\dot{\nu}_p(t - t_g)^2 + \frac{1}{6}\Delta\ddot{\nu}(t - t_g)^3 + \left[1 - \exp\left(-\frac{t - t_g}{\tau_d}\right)\right] \Delta\nu_d \tau_d, \quad (4)$$

where $\Delta\phi$ is the offset in pulsar phase, t_g is the glitch epoch, and $\Delta\nu_p$, $\Delta\dot{\nu}_p$ and $\Delta\ddot{\nu}$ are the respective permanent jumps in ν , $\dot{\nu}$ and $\ddot{\nu}$ relative to the pre-glitch solution. Finally, $\Delta\nu_d$ is the transient increment in the frequency that decays on a timescale τ_d . From these parameters one can calculate the degree of recovery, Q , which relates the transient and permanent jumps in frequency as $Q = \Delta\nu_d/\Delta\nu_g$. At last, two commonly used parameters in the literature are the instantaneous changes in the pulse frequency and its first derivative (at the glitch epoch), which can be described as

$$\Delta\nu_g = \Delta\nu_p + \Delta\nu_d \quad (5)$$

$$\Delta\dot{\nu}_g = \Delta\dot{\nu}_p - \frac{\Delta\nu_d}{\tau_d}. \quad (6)$$

Here we briefly review the detailed analysis (Zubieta et al. 2023) of the latest (#22 recorded) 2021 large Vela glitch, with $(\Delta\nu_g/\nu)_{2021} = 1.2 \times 10^{-6}$, providing an accurate description of the glitch characteristic epoch, jumps, and exponential recovery of 6.4 and 1 days times scales, (See Table 3 and Fig. 8).

2.3.1. Machine Learning analysis of the Vela Glitch Day: 2021, July 22 observations with A2

The observations on 2021 July 22 (the day of the glitch) with A2 are divided in three data parts. The first of those observations, starting at MJD 59417.65584, is about 52 minutes after the estimated occurrence of the glitch at MJD 59417.6194(2). The total observation time on July 22 is 2.65 h (divided into three observations) with a total SNR of 689. Since those three individual sub-observations contain enough pulses each to make a SOM analysis, we

TABLE 3
TIMING MODEL FOR THE 2021 JULY 22ND VELA GLITCH

Parameter	Value
PEPOCH (MJD)	59417.6193
F0(s ⁻¹)	11.18420841(1)
F1(s ⁻²)	-1.55645(4) × 10 ⁻¹¹
F2(s ⁻³)	6.48(1) × 10 ⁻²²
DM(cm ⁻³ pc)	67.93(1)
t _g (MJD)	59417.6194(2)
Δν _p (s ⁻¹)	1.381518(1) × 10 ⁻⁵
Δḡ _p (s ⁻²)	-8.59(4) × 10 ⁻¹⁴
Δḡ (s ⁻³)	1.16(3) × 10 ⁻²¹
Δν _{d1} (s ⁻¹)	3.15(12) × 10 ⁻⁸
τ _{d1} (days)	6.400(2)
Δν _{d2} (s ⁻¹)	9.9(6) × 10 ⁻⁸
τ _{d2} (days)	0.994(8)
Δφ	~ 0
Δν _g /ν	1.2469(5) × 10 ⁻⁶
Δḡ _g /ḡ	0.084(5)
Q ₁	0.00226(9)
Q ₂	0.0071(4)

proceed to consider them individually and independently. In search for more subtle details, we choose a six clusters study.

The results of those 6 SOM clustering studies are displayed in Fig. 9. We first observe that the right wing side of each mean cluster pulse seem all to superpose and that the sequence of those mean pulse clusters, with increasing amplitude, seem to appear earlier and earlier on average. The pulse width also shows a (weak) dependence on the cluster, being narrower for higher amplitude mean pulses. All these features, for the three observations covering from roughly 1–3.5 h after this large glitch seem to be similar to those well in between glitches, as we have observed in our previous analysis of the Vela pulses from January and March 2021 (Lousto et al. 2022).

2.3.2. Other glitching pulsars

The accuracy of our observations and procedures allowed us to determine two mini-glitches (the smallest recorded so far) in PSR 1048–5832, (#8 and #9 recorded), with $(\Delta\nu_g/\nu)_{2020} = 8.9 \times 10^{-9}$ and $(\Delta\nu_g/\nu)_{2021} = 9.9 \times 10^{-9}$, respectively.

On 2022 September 21, MJD=59839.4(5), a new glitch #9 in PSR J0742–2822 was reported by (Shaw et al. 2022). We have been able to confirm this glitch with our data (Zubieta et al. 2022b) and find relative

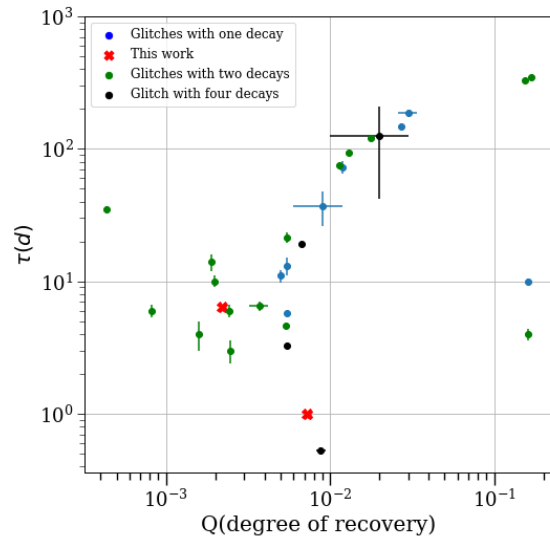


Fig. 8. Comparison of current and previous glitches decaying parameters for Vela pulsar.

jumps of $\Delta\nu/\nu = 4.29497(2) \times 10^{-6}$ and $\Delta\dot{\nu}/\dot{\nu} = 0.0510(7)$, making it the largest recorded glitch for this pulsar.

Also, on 2022 December 22, MJD=59935.1(4), we detected a new glitch in PSR J1740–3015 that was reported in (Zubieta et al. 2022a). We found a relative jump of $\Delta\nu/\nu = 3.32(3) \times 10^{-7}$ and plan to continue monitoring PSR J1740–3015 to improve the post-glitch timing solution.

(See E. Zubieta’s contribution to this volume for other details on the glitching pulsar observations mentioned here).

This concludes our review of the main PuMA results and we now discuss the new projects underway.

3. FUTURE PROJECTS AND CONCLUSIONS

3.1. Single-pulse timing

We presented the first detailed analysis of the 2019/2020 observational campaign towards the bright millisecond J0437–4715 using the two antennas at IAR’s observatory. This data set comprises now over three additional years of high-cadence (up to daily) observations with both antennas, A1 and A2. By both improving the time baseline of observations, (including the additional three years of data) and combining it with a future single pulse analysis, we may achieve up to factors 2-3 improvements in the timing accuracy (Kerr 2015). We recall here that one of the main results of the Vela single pulse analysis of (Lousto et al. 2022) was the narrower nature of the high amplitude pulses clusters, which,

if translated to J0437–4715, would lead to notable timing improvements.

It is worth noting here that there are several difficulties to overcome in order to further dramatically improve the timing of millisecond pulsars at lower frequencies, among them the accurate modeling of the dispersion and Faraday’s rotation of the interstellar media scaling like the inverse frequency squared, $1/\nu^2$, and the scattering and scintillation scaling like $1/\nu^4$.⁴ Additionally one has to account for the time dependence of the Dispersion measure (DM), solar wind, and the frequency evolution of the pulsar profile.

Ongoing and future hardware upgrade of IAR’s antennas, such as installing larger-bandwidth boards (from the current 56MHz (Ettus¹⁰) to 400MHz (ROACH¹¹)), promise to expand IAR’s observational capabilities and improve its achievable timing precision by raising sensitivity at least by a factor 3. Thus, with the future improvements in IAR’s antennas receivers, which include a combination of broader bandwidth and reduction of system temperature, it will be possible to study the dynamical spectra of single pulses for other pulsars of interest, such as the glitching PRS J1644-4559 and J0738-4042, and the millisecond pulsar J0437-4715 to contribute to improve pulsar timing arrays data in order to detect a stochastic gravitational waves background. We display some of the pulse properties of this primary choice of pulsars accessible to IAR for single-pulse studies in Table 4.

We recall here the standard formula for the expected signal-to-noise ratio (S/N; Lorimer & Kramer 2012):

$$S/N \lesssim S_{\text{mean}} \frac{\sqrt{n_p t_{\text{obs}} B}}{GT_{\text{sys}}} \sqrt{\frac{P-W}{W}}, \quad (7)$$

where S_{mean} , P , and W are the mean flux density, period and equivalent width of the pulses, respectively, G , B , n_p , and T_{sys} are the antenna gain, bandwidth, number of polarizations, and system temperature, respectively; with t_{obs} , the effective observing time. In table 4 we used the data from the ATNF catalogue (<http://www.atnf.csiro.au/people/pulsar/psrcat/>) to estimate a relative $S/N = S1400\sqrt{P/W - 1}$ (arbitrary normalization) and $P0/W$ as a measure of the relative extension of the pulse over the period. We use the notation PSRJ: Pulsar name based on J2000 coordinates, P0: Barycentric period of the pulsar (s),

¹⁰<https://www.ettus.com/all-products/usrp-b205mini-i-board/>

¹¹<https://www.digicom.org/roach-board.html>

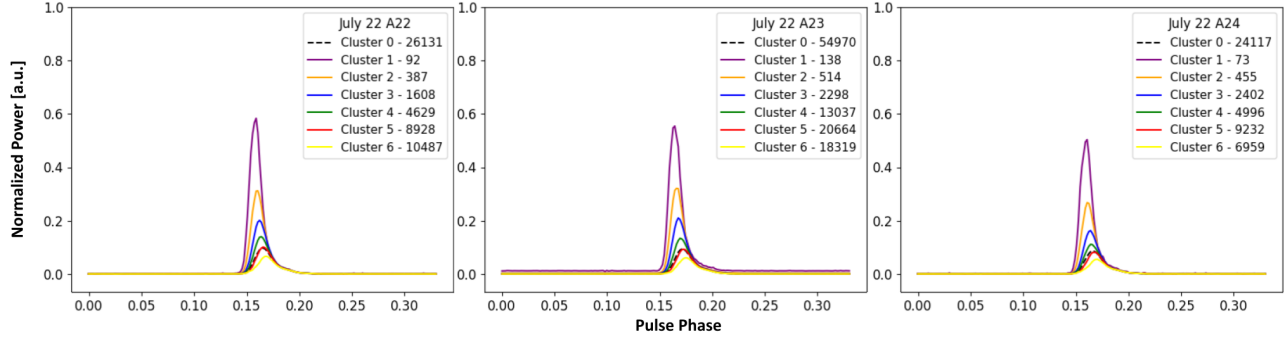


Fig. 9. Mean cluster pulses for 2021 July 22 three successive observations (roughly from 1 to 3.5 h after the glitch) with Antenna 2 for 6 SOM clusters with VAE reconstruction. 200 (out of total 611) phase bins were taken around the mean peak of each day to perform the single-pulse analysis on.

TABLE 4

IAR'S ACCESSIBLE PULSARS FOR SINGLE-PULSE STUDIES.

PSR J2000	P0 (s)	S1400 (mJy)	G #	W50 (ms)	W10 (ms)	P0/W50	P0/W10	S/N (W50)	S/N (W10)
J0437-4715	0.005757	150.20	*	0.141	1.020	40.83299	5.644561	947.963	323.6997
J0738-4042	0.374921	112.60	*	25.000	39.000	14.99683	9.613352	421.2629	330.4643
J0835-4510	0.089328	1050.00	22	1.700	3.800	52.54611	23.50747	7538.54	4981.414
J1644-4559	0.455078	300.00	4	8.000	13.323	56.88478	34.15734	2242.684	1727.472

S1400: Mean flux density at 1400 MHz (mJy), G (NGlt): Number of glitches observed for the pulsar, W50: Width of pulse at 50% of peak (ms), W10: Width of pulse at 10% (ms).

3.2. Intelligent Fast Radio Burst searches

With thousands of good quality hours of pulsar observations it is interesting to see if the data contains also FRB (Petroff et al. 2019) signals. In particular, machine learning techniques have been developed to perform massive searches of FRB (Zhang et al. 2018) and its classification (Connor & van Leeuwen 2018; Wagstaff et al. 2016) using supervised (Luo et al. 2022) and unsupervised methods (Chen et al. 2021; Zhu-Ge et al. 2022). A most practical implementation for fast transient classification (Agarwal et al. 2020) is the Fetch code: <https://github.com/devanshkv/fetch>. Another useful tool is the synthetic FRB generator: <https://gitlab.com/houben.1jm/frb-faker> to train FRB searches and classification. A Living Theory Catalogue for Fast Radio Bursts with a review of the numerous existing theories to model FRBs is reported in (Platts et al. 2019).

(For more on magnetars and FRB projects at IAR, see also S.B. Araujo Furlan's presentation in this volume).

3.3. Lower frequencies observations

IAR's Multipurpose Interferometer Array (MIA) is the only project of its kind in South America: a versatile low frequency interferometer (100 MHz - 2 GHz) designed to investigate transient sources and non-thermal cosmic radiation from the Southern Hemisphere. MIA will initially consists of a 16 antennas array of 5 meters in diameter each, distributed over a baseline of 50Km in order to obtain an angular resolution of at least 1.5 seconds of arc in the L-Band.

Regarding the use of MIA for pulsar observations, we may consider that in order for MIA to have a collecting surface equivalent to the 30 meters diameter A1 and A2 at IAR, one should have 36×5 meters MIA antennas. This number can be reduced to about 24 dishes if they use solid slabs instead of wired ones, since the former raise the gain to about 60% from the later 40%. Another gain can be obtained if individually optimized dedicated receivers can be used for each frequency sub-bands 0.3-1 GHz¹², 1-2 GHz¹³, and 2-4 GHz¹⁴. Those 24

¹²<https://www.pasternack.com/5-section-high-pass-filter-300-mhz-1000-mhz-passband-700-mhz-pe8718-p.aspx>

¹³<https://www.pasternack.com/11-section-band-pass-filter-1-2-ghz-passband-1000-mhz-pe87f1012-p.aspx>

¹⁴<https://www.pasternack.com/11-section-band-pass-filter-2-4-ghz-passband-2-ghz-pe87f1013-p.aspx>

MIA antennas could be developed in three stages of 4 pre-series + 12 series + 8 additional to complete an hexagonal pattern of two 3 by 4 sub-arrays as displayed on top of Fig. 10. For instance, setting those 24 MIA antennas $D = 2\text{km}$ apart would cover about a land region of $S = 15D^2 = 60\text{km}^2$ and a baseline of $B = 5D = 10\text{km}$. This square blocks configurations of 4 antennas allow for an interferometric locking with total cancellation of phase and amplitude. An alternative configuration, based on the initial prototype of 3 antennas, is to place them in equilateral triangles in an hexagonal pattern as displayed in the bottom Fig. 10. The MIA19 with separations of $d = 2\text{km}$ between dishes would cover a ground area of about $S = 6\sqrt{3}d^2 = 42\text{km}^2$ and a radial baseline of $B = 4d = 8\text{km}$. The basic interferometric pattern would thus be similar to that studied for the space antenna LISA with three equilaterally placed spacecrafts in orbit around the sun (Amaro-Seoane et al. 2017).

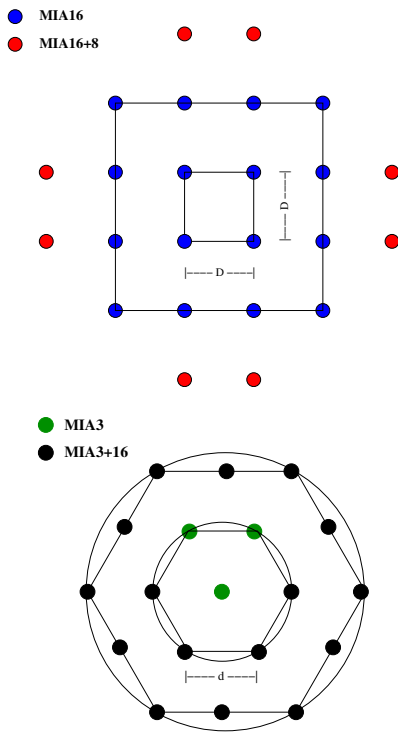


Fig. 10. On top the MIA24 configuration and on bottom an alternative MIA19 for interferometric pulsar observations.

By accessing lower frequencies, MIA would allow to include new glitching pulsars to our survey. Pulsars that typically have negative spectral index emit much more in the 400MHz band than in the

TABLE 5

MIA'S ACCESSIBLE GLITCHING PULSARS

PSR	P0	S400	S1400	G	S/N
J2000	(s)	(mJy)	(mJy)	#	@400
J0820-1350	1.238	102.0	6.00	2	741.4
J1602-5100	0.864	45.0	8.23	1	643.9
J1836-1008	0.563	54.0	4.80	1	458.4
J1740-3015	0.607	24.6	8.90	37	349.0
J1703-4851	1.396	22.0	1.40	1	246.9
J1835-1106	0.166	30.0	2.50	1	193.4
J1705-1906	0.299	29.0	5.66	4	172.7
J1720-1633	1.566	13.0	1.10	1	147.9
J1705-3423	0.255	31.0	5.30	3	139.6
J1328-4357	0.533	18.0	4.40	1	123.9
J0846-3533	1.116	16.0	5.00	1	121.6
J1257-1027	0.617	12.0	1.20	1	115.4
J1320-5359	0.279	18.0	2.10	2	105.6
J1757-2421	0.234	20.0	7.20	1	94.68
J0758-1528	0.682	8.2	2.60	1	78.85
J0905-5127	0.346	12.0	1.05	2	77.54
J1123-6259	0.271	11.0	0.51	1	70.79
J1803-2137	0.134	23.0	9.60	5	70.07
J0729-1836	0.510	11.2	1.90	2	66.67
J1824-2452A	0.003	40.0	2.30	1	58.54
J1141-3322	0.291	8.0	1.60	1	58.23
J1743-3150	2.415	6.6	2.10	1	47.89
J1801-2451	0.125	7.8	1.46	7	39.02
J1730-3350	0.139	9.2	4.30	3	36.81

1400MHz band we use to observe with A1 and A2. Using the ATNF data base we can find (See Table 5) two dozen glitching pulsars with sufficient S/N to be observed by MIA that currently cannot be accurately followed with A1 and A2. The angular resolution of MIA in the configurations of Fig. 10 with $B > 1\text{km}$, would beat the angular resolution of $1'$ versus the current $30'$ of A1 and A2 at 1400MHz.

(See G. Gancio's contribution to this volume for a description of the MIA project carried out at IAR).

Let us conclude here with a quote from a most inspiring author, *Pensar es olvidar diferencias, es generalizar, abstraer.* "To think is to forget a difference, to generalize, to abstract.", from 'Funes the Memorious', *Ficciones* — Jorge Luis Borges (Borges 1999).

Acknowledgements

COL gratefully acknowledge the National Science Foundation (NSF) for financial support from Grants No. PHY-1912632, PHY-2207920 and RIT-COS 2021-DRIG grant. JAC and FG are CONICET researchers. JAC is a María Zambrano researcher fellow funded by the European Union - NextGenerationEU- (UJAR02MZ). This work received financial support from PICT-2017-2865 (ANPCyT) and PIP 0113 (CONICET). JAC and FG were also supported by grant PID2019-105510GB-C32/AEI/10.13039/501100011033 from the Agencia Estatal de Investigación of the Spanish Ministerio de Ciencia, Innovación y Universidades, and by Consejería de Economía, Innovación, Ciencia y Empleo of Junta de Andalucía as research group FQM-322, as well as FEDER funds.

REFERENCES

- Agarwal, D., Aggarwal, K., Burke-Spolaor, S., Lorimer, D. R., & Garver-Daniels, N. 2020, *MNRAS*, 497, 1661
- Amaro-Seoane, P. et al. 2017
- Bajaja, E., Arnal, E. M., Larrarte, J. J., Morras, R., Poppel, W. G. L., & Kalberla, P. M. W. 2005, *Astron. Astrophys.*, 440, 767
- Borges, J. L. 1999, *Collected Fictions* (London: Penguin Classics Deluxe Edition)
- Chen, B. H., Hashimoto, T., Goto, T., Kim, S. J., Santos, D. J. D., On, A. Y. L., Lu, T.-Y., & Hsiao, T. Y. Y. 2021, *Mon. Not. Roy. Astron. Soc.*, 509, 1227
- Connor, L. & van Leeuwen, J. 2018, *Astron. J.*, 156, 256
- Cordes, J. M. 2000, arXiv e-prints, astro
- Cordes, J. M. & Chernoff, D. F. 1997, *ApJ*, 482, 971
- Ellis, J. A., Vallisneri, M., Taylor, S. R., & Baker, P. T. 2019, ENTERPRISE: Enhanced Numerical Toolbox Enabling a Robust Pulsar Inference Suite
- Gancio, G., Lousto, C. O., Combi, L., del Palacio, S., López Armengol, F. G., Combi, J. A., García, F., Kornecki, P., Müller, A. L., Gutiérrez, E., Hauscarriaga, F., & Mancuso, G. C. 2020, *A&A*, 633, A84
- Hazboun, J., Romano, J., & Smith, T. 2019, *Journal of Open Source Software*, 4, 1775 [LINK]
- Kalberla, P. M. W., Burton, W. B., Hartmann, D., Arnal, E. M., Bajaja, E., Morras, R., & Poppel, W. G. L. 2005, *Astron. Astrophys.*, 440, 775
- Kerr, M. 2015, *Mon. Not. Roy. Astron. Soc.*, 452, 607
- Kingma, D. P. & Welling, M. 2014, *Auto-Encoding Variational Bayes*
- Krishnamohan, S. & Downs, G. S. 1983, *ApJ*, 265, 372
- Lopez Armengol, F. G., Lousto, C. O., del Palacio, S., Garcia, F., Combi, L., Combi, J. A., Gancio, G., Mueller, A. L., & Kornecki, P. 2019, *The Astronomer's Telegram*, 12482, 1
- Lorimer, D. R. & Kramer, M. 2012, *Handbook of Pulsar Astronomy* (Cambridge University Press)
- Lousto, C. O., Missel, R., Prajapati, H., Sosa Fiscella, V., Armengol, F. G. L., Gyawali, P. K., Wang, L., Cahill, N. D., Combi, L., Palacio, S. d., Combi, J. A., Gancio, G., García, F., Gutiérrez, E. M., & Hauscarriaga, F. 2022, *MNRAS*, 509, 5790
- Lousto, C. O., Zlochower, Y., & Campanelli, M. 2017, *ApJ*, 841, L28
- Luo, J.-W., Zhu-Ge, J.-M., & Zhang, B. 2022, *Mon. Not. Roy. Astron. Soc.*, 518, 1629
- Mcculloch, P., Klekociuk, A., Hamilton, P., & Royle, G. 1987, *Australian Journal of Physics*, 40, 725
- Petroff, E., Hessels, J. W. T., & Lorimer, D. R. 2019, *A&A Rev.*, 27, 4
- Platts, E., Weltman, A., Walters, A., Tendulkar, S. P., Gordin, J. E. B., & Kandhai, S. 2019, *Phys. Rept.*, 821, 1
- Shaw, B., Mickaliger, M. B., Stappers, B. W., Lyne, A. G., Keith, M. J., Weltevrede, P., & Basu, A. 2022, *The Astronomer's Telegram*, 15622, 1
- Sosa Fiscella, V., Combi, L., del Palacio, S., Lousto, C. O., Combi, J. A., Gancio, G., García, F., Gutiérrez, E., Hauscarriaga, F., Kornecki, P., López Armengol, F. G., Mancuso, G. C., Müller, A. L., & Simaz Bunzel, A. 2021, *Boletín de la Asociación Argentina de Astronomía La Plata Argentina*, 62, 268
- Testori, J. C., Reich, P., Bava, J. A., Colomb, F. R., Hurrell, E. E., Larrarte, J. J., Reich, W., & Sanz, A. J. 2001, *Astron. Astrophys.*, 368, 1123
- Wagstaff, K. L., Tang, B., Thompson, D. R., Khudikyan, S., Wyngaard, J., Deller, A. T., Palaniswamy, D., Tingay, S. J., & Wayth, R. B. 2016, *Publ. Astron. Soc. Pac.*, 128, 084503
- Zhang, Y. G., Gajjar, V., Foster, G., Siemion, A., Cordes, J., Law, C., & Wang, Y. 2018, *Astrophys. J.*, 866, 149
- Zhu-Ge, J.-M., Luo, J.-W., & Zhang, B. 2022, *Mon. Not. Roy. Astron. Soc.*, 519, 1823
- Zubieta, E., Araujo Furlan, S. B., Palacio, S. d., Garcia, F., Gancio, G., Lousto, C. O., Combi, J. A., & Combi, L. 2022a, *The Astronomer's Telegram*, 15838, 1
- Zubieta, E., Del Palacio, S., Garcia, F., Gancio, G., Lousto, C. O., Combi, J. A., Combi, L., Gutierrez, E., Lopez-Armengol, F. A., Simaz Bunzel, A., & Sosa-Fiscella, V. 2022b, *The Astronomer's Telegram*, 15638, 1
- Zubieta, E., Missel, R., Sosa Fiscella, V., Lousto, C. O., del Palacio, S., López Armengol, F. G., García, F., Combi, J. A., Wang, L., Combi, L., Gancio, G., Negrelli, C., & Gutiérrez, E. M. 2023, *MNRAS*